



1 Poleward shift of the North Pacific storm track driven by springtime 2 East Asian dust heating

3 Anbao Zhu^{1, 2, 3}, Xin Huang^{1, 2}, Haiming Xu³, Jiechun Deng³, Lian Xue⁴, Zilin Wang^{1, 2}, Ke Ding^{1, 2},
4 Tianshuai Li^{1, 2}, Aijun Ding^{1, 2}

5 ¹Joint International Research Laboratory of Atmospheric and Earth System Sciences, School of Atmospheric Sciences, Nanjing
6 University, Nanjing 210023, China

7 ²State Key Laboratory of Severe Weather Meteorological Science and Technology, Nanjing University, Nanjing 210023,
8 China

9 ³School of Atmospheric Sciences, Nanjing University of Information Science & Technology, Nanjing 210044, China

10 ⁴Nanjing-Helsinki Institute in Atmospheric and Earth System Sciences, Nanjing University, Suzhou 215163, China

11 *Correspondence to:* Xin Huang (xinhuang@nju.edu.cn)

12 **Abstract.** The North Pacific storm track shapes precipitation and temperature patterns over the Arctic and western North
13 America, yet how its sensitivity to springtime East Asian dust remains poorly understood. Based on the Modern-Era
14 Retrospective analysis for Research and Applications, Version 2 (MERRA-2) reanalysis data from 1980 to 2022, we find that
15 anomalously high springtime East Asian dust loading is robustly associated with a systematic poleward shift of the North
16 Pacific storm track on interannual timescales. The physical mechanism proceeds through a clear causal chain. In details,
17 shortwave absorption by the trans-Pacific dust plume warms the mid-troposphere between 850 and 400 hPa, exciting an
18 anomalous anticyclonic circulation over the North Pacific. This thermal perturbation restructures the meridional temperature
19 gradient and shifts the zone of maximum Eady growth rate poleward, thereby relocating the preferred region for baroclinic
20 eddy development to higher latitudes. The Weather Research and Forecasting model coupled with Chemistry (WRF-Chem)
21 sensitivity experiments reproduce both the spatial pattern and sign of the storm track response, confirming that dust shortwave
22 absorption is sufficient to drive the observed displacement. These findings demonstrate that natural dust aerosols can modulate
23 large-scale North Pacific atmospheric dynamics and suggest that springtime dust variability should be considered in regional
24 climate assessments.

25



26 **1 Introduction**

27 Storm tracks are regions where extratropical cyclones preferentially form, develop, and dissipate (Shaw et al., 2016). They are
28 largely characterized by transient eddy activities that drive midlatitude atmospheric circulation (Chang and Lee and Swanson,
29 2002). The North Pacific storm track is a major branch of the Northern Hemisphere storm track system. It originates near the
30 East Asian coastal stationary trough (Blackmon, 1976) and is sustained by baroclinic instability that converts mean-flow
31 available potential energy into eddy kinetic energy through the equator-to-pole temperature gradient (Simmons and Hoskins,
32 1978; Chang and Lee and Swanson, 2002). The North Pacific storm track plays a key role in the climate system. It accounts
33 for much of the poleward transport of heat, moisture, and momentum across the North Pacific basin, delivering them into the
34 Arctic and western North America (Trenberth and Stepaniak, 2003; Salathé Jr., 2006). Through this transport, it heavily
35 influences regional weather patterns and midlatitude extreme events, including severe winds and heavy precipitation over both
36 the North Pacific and western North America (Salathé Jr., 2006; Pfahl et al., 2014; Chemke and Yuval, 2026). Therefore, it is
37 essential to understand its variability for regional weather forecasting and climate prediction (Shaw et al., 2016).

38
39 East Asia is one of the world's major source regions of mineral dust aerosols (Kok et al., 2023). Every spring, intense dust
40 plumes originate from the Taklimakan and Gobi Deserts and are transported eastward by mid-latitude westerlies, forming a
41 extensive aerosol belt over the North Pacific (Huang et al., 2014; Yu et al., 2019). Unlike predominantly scattering aerosols,
42 mineral dust exhibits substantial shortwave absorption due to its iron oxide content (Sokolik and Toon, 1999), producing
43 notable radiative heating within the atmospheric column (Chen et al., 2017). This dust radiative heating can significantly
44 modulate large-scale atmospheric circulation, weather systems and air pollution, such as the Indian summer monsoon (Lau
45 and Kim and Kim, 2006; Jin et al., 2021), Atlantic hurricanes (Sun and Zhao, 2020; Xian et al., 2020), Mongolian cyclones
46 (Chen et al., 2023), and Particle and Ozone Pollution in East China (Wang et al., 2019). Observational records also show a
47 recent increase in severe dust storms over East Asia (Yin et al., 2026; Yin et al., 2022), leading to substantial perturbations on
48 radiative energy balance (Gui et al., 2022). The increasing frequency of these extreme events underscores the need to evaluate
49 the climatic impacts of springtime dust variability.

50
51 Although the influence of aerosols on the North Pacific storm track has received increasing attention, most previous studies
52 have focused on wintertime anthropogenic aerosols. Modelling studies demonstrate that East Asian anthropogenic emissions
53 induce an equatorward shift of the subtropical jet and the North Pacific storm track primarily by cooling the surface through
54 aerosol–radiation interactions (Ming and Ramaswamy and Chen, 2011; Zhou and Deng, 2013; Wang and Jiang and Su, 2015;
55 Liu et al., 2019). Furthermore, through aerosol–cloud interactions, anthropogenic aerosols that act as cloud condensation nuclei
56 enhance deep convective clouds and intensify mid-latitude cyclones, resulting in approximately 7% more precipitation within
57 the Pacific storm track (Zhang et al., 2007; Wang and Zhang and Saravanan, 2014; Wang et al., 2014). However, during spring,
58 when the East Asian–North Pacific aerosol regime transitions from anthropogenic-dominated to dust-dominated (Zhu et al.,



59 2007; Bao and Wen and Wu, 2009), the storm track response to springtime dust remains largely unexplored. Notably, satellite-
60 based analyses reveal that wintertime East Asian aerosols significantly enhance deep convective clouds in the North Pacific
61 storm track. Interestingly, this signal disappears in spring, even though the aerosol optical depth (AOD) reaches its annual
62 maximum during this season (Bender and Ramanathan and Tselioudis, 2012). This seasonal contrast suggests that springtime
63 dust aerosols may exert fundamentally different effects on the storm track compared to wintertime anthropogenic aerosols.

64

65 This study investigates the interannual impact of springtime East Asian dust aerosols on the North Pacific storm track by using
66 reanalysis data from 1980 to 2022, along with modelling sensitivity experiments. Specifically, this research aims to determine
67 how East Asian dust aerosols affect the North Pacific storm track during spring on an interannual timescale and to identify the
68 underlying physical mechanisms. The remainder of the paper is organized as follows. Section 2 describes the data and
69 methodology. Section 3 presents the observational evidence and physical mechanisms, which are further verified by modelling
70 simulations. Finally, Section 4 provides the conclusions and discussion.

71 **2 Methodology**

72 **2.1 Data**

73 The primary dataset used in this study is the Modern Era Retrospective analysis for Research and Applications, Version 2
74 (MERRA-2). It is provided by the National Aeronautics and Space Administration Global Modeling and Assimilation Office
75 (GMAO) (Gelaro et al., 2017). We utilize MERRA-2 for both aerosol and meteorological fields to ensure dynamic consistency.
76 The data are provided on a 0.5° by 0.65° spatial grid with 72 vertical levels. The MERRA-2 aerosol data are generated using
77 the Goddard Chemistry Aerosol Radiation and Transport (GOCART) model coupled with the GEOS-5 data assimilation
78 system. The GOCART model simulates five aerosol species: dust, black carbon, organic carbon, sulfate, and sea salt.
79 Furthermore, GEOS-5 assimilates bias-corrected AOD from various observation platforms. These include the AVHRR
80 instrument over oceans (Heidinger et al., 2014), the MODIS instrument from Terra and Aqua satellites (Levy et al., 2010), the
81 MISR instrument over desert regions (Kahn et al., 2005), and ground-based AERONET stations (Holben et al., 1998).

82

83 We use the monthly mean dust column mass density from MERRA-2 to represent the atmospheric dust loading over East Asia
84 and the North Pacific. Recent evaluations indicate that MERRA-2 slightly underestimates absolute dust concentrations
85 compared to ground-based retrievals. However, it exhibits a high temporal correlation with station observations (Zhang et al.,
86 2024). Because MERRA-2 accurately captures the spatiotemporal variability of dust aerosols, this product is widely used in
87 climate analyses (Wang and Lau and Wang, 2021; Li et al., 2023; Fu et al., 2026). We also use the AOD from the 1° MODIS
88 Terra Level-3 monthly product (MOD08_M3) (Gupta et al., 2016) to evaluate the model's simulation of dust aerosol spatial
89 distribution. Alongside the aerosol data, we utilize MERRA-2 atmospheric variables, including geopotential height, air



90 temperature, vertical velocity, and horizontal winds. Additionally, we obtain monthly precipitation data on a 2.5° by 2.5° grid
91 from the Climate Prediction Center Merged Analysis of Precipitation (CMAP) dataset (Xie and Arkin, 1997).

92 **2.2 Storm track definition and statistical methods**

93 We define storm track activity using two metrics. The first is the upper-tropospheric transient eddy geopotential height variance
94 at 300 hPa ($Z'Z'_{300}$). The second is the lower-tropospheric transient eddy meridional heat flux at 850 hPa ($V'T'_{850}$). Together,
95 these two metrics provide a comprehensive three-dimensional representation of storm track activity (Chang and Lee and
96 Swanson, 2002). We calculate the transient variance and heat flux using daily MERRA-2 data. A 2.5–6-day bandpass filter is
97 applied to these daily data to isolate synoptic-scale fluctuations. To quantify atmospheric baroclinicity, we compute the
98 maximum Eady growth rate (EGR) defined as:

$$99 \quad \sigma_{EGR} = 0.31 \frac{f}{N} \left| \frac{\partial U}{\partial z} \right|,$$

100 where f is the Coriolis parameter, N is the Brunt-Väisälä frequency, and $\left| \frac{\partial U}{\partial z} \right|$ is the vertical wind shear (Lindzen and Farrell,
101 1980).

102

103 All datasets used in this study span the period from 1980 to 2022. To isolate interannual variability, we apply Fourier analysis
104 to remove the first four harmonics from the time series. This procedure effectively filters out interdecadal background signals
105 (Awan and Bae, 2016; Zhu et al., 2021). On interannual timescales, the variability of the North Pacific storm track is closely
106 linked to the El Niño Southern Oscillation (ENSO). During El Niño events, the Pacific storm track typically shifts equatorward
107 and extends downstream (Seager et al., 2010; Jiang and Deng and Li, 2013). To explicitly isolate the physical impacts of dust
108 aerosols from these ENSO-driven circulation changes, we employ partial regression methods (Cai et al., 2011; Liguori et al.,
109 2022). Specifically, we use the Niño 3.4 index as the ENSO indicator and linearly regress out its concurrent spring signal from
110 all variables prior to the dust-storm track regression analysis. Furthermore, we use empirical orthogonal function (EOF)
111 analysis to extract dominant variability patterns. Finally, the statistical significance of all correlation and regression results is
112 evaluated using a two-tailed Student's t -test.

113 **2.3 Model and experimental design**

114 We use the Weather Research and Forecasting model coupled with Chemistry (WRF-Chem) version 3.9.1. This model
115 simulates meteorological processes and dust activities over East Asia and the North Pacific during the boreal spring. The
116 simulation domain spans from East Asia to the central North Pacific. It employs a regular latitude and longitude projection
117 with 381 by 131 grid points centred at 50°N and 160°E (Figure S1). The horizontal resolution is 0.5° by 0.5°, which
118 corresponds to approximately 55 km. The vertical grid contains 45 levels from the surface up to 50 hPa. Initial and boundary
119 meteorological conditions are derived from the National Centres for Environmental Prediction (NCEP) Final Analysis (FNL)



120 data (Ncep, 2000). These data have a 1° spatial resolution and update every 6 hours. Additionally, we incorporate sea surface
121 temperature data from the NCEP real time global sea surface temperature analysis.

122

123 We configure the model with a comprehensive suite of physical and chemical parameterization schemes. Table 1 summarizes
124 these specific options. For cloud and precipitation processes, we select the Lin microphysics scheme (Lin and Colle, 2011)
125 and the Grell-3D ensemble cumulus scheme (Grell, 1993; Grell and Dévényi, 2002). The Rapid Radiative Transfer Model for
126 General Circulation Models (RRTMG) calculates both shortwave and longwave radiation while accounting for aerosol
127 radiative effects (Iacono et al., 2008). Planetary boundary layer processes are parameterized using the Yonsei University (YSU)
128 scheme (Hong and Noh and Dudhia, 2006). This is coupled with the MM5 Monin-Obukhov surface layer scheme and the
129 Unified Noah land surface model to represent surface physics and land atmosphere interactions (Pahlow and Parlange and
130 Porté-Agel, 2001; Chen et al., 2010). For atmospheric chemistry, we employ the second generation Regional Acid Deposition
131 Model (RADM2) for gas phase reactions (Stockwell et al., 1990), alongside the Fast-J photolysis scheme. The GOCART
132 module simulates aerosol chemistry (Chin et al., 2002). Aerosol optical properties are computed using the Maxwell Garnett
133 approximation (Bohren and Huffman, 1983). Finally, we adopt the Shao 2004 dust emission scheme (Shao, 2004). Previous
134 studies demonstrate its excellent performance in simulating dust emissions and the spatiotemporal variability of dust mass
135 concentrations over East Asia (Tang et al., 2018; Zhao et al., 2020; Idrissa et al., 2024).

136

Table 1. WRF-Chem modeling parameterization option settings

Option name	Scheme
Longwave radiation	RRTMG
Shortwave radiation	RRTMG
Microphysics	Lin
Boundary layer	YSU
Cumulus	Grell-3D
Land surface	Unified Noah
Surface layer	MM5 Monin-Obukhov
Aerosol chemistry	GOCART
Gas chemistry	RADM2
Photolysis	Fast-J
Dust emissions	Shao2004

137

138 We design two sets of simulations to investigate the radiative and dynamical impacts of dust aerosols on the North Pacific
139 storm track. The control experiment (CTRL) incorporates full dust emissions. In contrast, the sensitivity experiment (NoDust)
140 completely disables dust emissions. We attribute the atmospheric differences between the CTRL and NoDust simulations

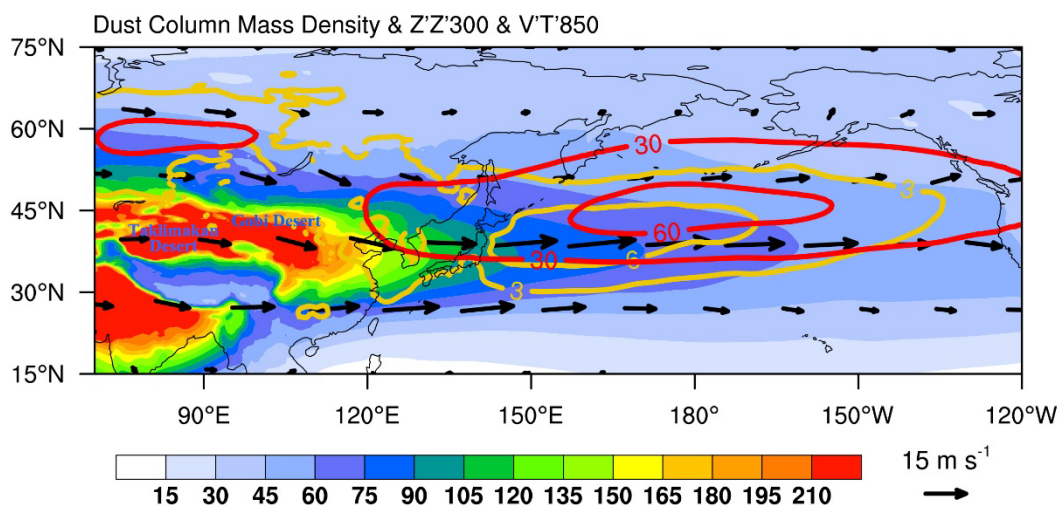


141 directly to the effects of dust aerosols. We select the year 2018 as our study period because the East Asian dust loading during
 142 this year significantly exceeded the climatological mean (Figure 2b). To enhance the statistical robustness of our results, we
 143 conduct seven ensemble members for each experiment. These ensemble members are initialized one day apart from 19 to 25
 144 February 2018. All simulations conclude on 31 May 2018. We treat February as the model spin-up period and exclude it from
 145 the final analysis. Consequently, our analysis focuses strictly on the boreal spring season from March to May 2018. We
 146 acknowledge that this single-year simulation cannot fully capture the interannual variability present in the reanalysis. The
 147 WRF-Chem experiments are therefore designed as a process-level verification of the proposed physical mechanism rather than
 148 as an independent confirmation of the interannual statistical relationship.

149 3 Results

150 3.1 Observational link between dust and the storm track

151 As shown in Figure 1, Asian dust loading peaks over the Taklimakan and Gobi deserts and extends eastward over the North
 152 Pacific, spatially overlapping with the storm track region characterized by $Z'Z'_{300}$ and $V'T'_{850}$. This spatial collocation
 153 suggests the potential for dynamical interactions between dust aerosols and storm track activity, motivating the present
 154 investigation. To further characterize the spatiotemporal variability of East Asian dust loading, we apply EOF analysis to the
 155 spring dust column mass density anomalies over 1980–2022, with spring defined as March–April–May (MAM). The leading
 156 EOF mode (EOF1; Figure 2a) explains approximately 46% of the total variance and is characterized by same-sign loading
 157 across East Asia, with the largest amplitude over the Taklimakan and Gobi deserts. This pattern is consistent with the known
 158 structure of dust variability, in which the most pronounced fluctuations are concentrated over the major source regions (Guo
 159 et al., 2019).



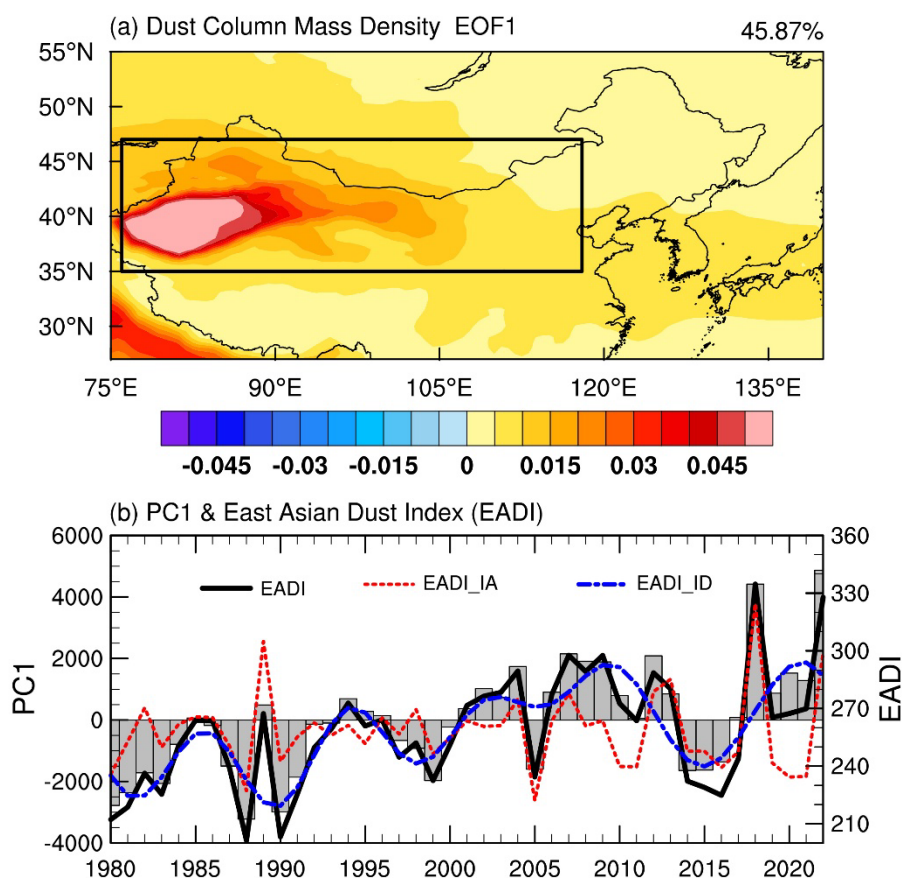
160

161 **Figure 1.** Spatial distribution of climatological spring (March–April–May, MAM) mean dust column mass density (shading; mg m^{-2}),
 162 500 hPa wind (vector; m s^{-1}), transient eddy meridional heat flux at 850 hPa ($V'T'_{850}$, EMHF; orange contour with interval of 3



163 K m s^{-1}) and transient variances of geopotential height at 300 hPa ($Z'Z'_{300}$, EGHV ; red contour with interval of 30 dagpm²)
 164 averaged over 1980–2022.

165 Based on this spatial pattern, we define an East Asian dust index (EADI) as the area-averaged dust column mass density over
 166 the key region (35°–47°N, 76°–118°E; black box in Figure 2a) where the variance is largest. The resulting EADI is highly
 167 correlated with the EOF1 principal component (PC1), with a correlation coefficient exceeding 0.97 (Figure 2b), confirming
 168 that the EADI effectively captures both interannual and interdecadal variability of spring East Asian dust loading. The temporal
 169 evolution of EADI reveals two distinct timescales of variability. On the interdecadal timescale, an abrupt increase occurs
 170 around 1999, coinciding with a phase reversal in PC1 from negative to positive, which has been linked to changes in 10-m
 171 wind speed over dust source regions (Guo et al., 2019). On the interannual timescale, the EADI exhibits substantial year-to-
 172 year fluctuations, reflecting the large variability in dust emission and transport processes (Yu et al., 2019). Given that
 173 interannual variability constitutes an important component of total dust variability, this study focuses on the North Pacific
 174 storm track response to the interannual dust variability over East Asia. Unless otherwise stated, all variables discussed hereafter
 175 refer to their interannual components.



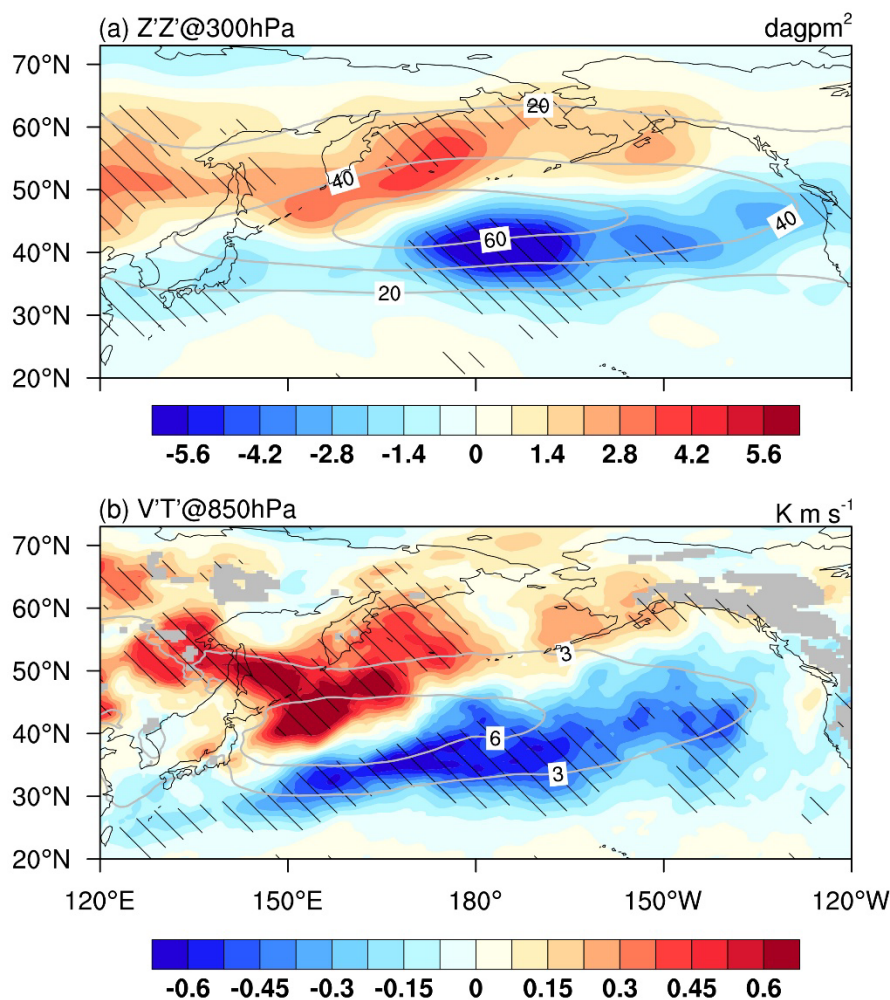
176

177 **Figure 2. (a) Spatial pattern (shading) and (b) principal component (gray bars) of the first EOF mode of MAM mean dust column**
 178 **mass density over East Asia during 1980–2022. The spring East Asian dust index (EADI; black solid line) defined as dust column**



179 **mass density averaged over East Asia [76°–118°E, 35°–47°N; the black box in (a)] is also plotted in (b), together with its interannual**
180 **component (EADI_IA; red dashed line) and interdecadal component (EADI_ID; blue dashed line).**

181 To investigate the interannual relationship between East Asian dust loading and the North Pacific storm track, Figure 3 presents
182 the regression of anomalous $Z'Z'_{300}$ and $V'T'_{850}$ onto the interannual component of the EADI. Both fields exhibit a
183 meridional dipole pattern that is approximately symmetric about the climatological storm track axis, suggesting a systematic
184 poleward displacement of storm track activity during high-dust springs (relative to low-dust springs). Specifically, significant
185 negative $Z'Z'_{300}$ anomalies appear over the East China Sea and the east-central North Pacific, with the largest reduction
186 reaching approximately 7.5 dagpm² (~15% of the climatological mean). Meanwhile, significant positive anomalies exceeding
187 2.0 dagpm² (more than 8% of the climatological mean) emerge over eastern Siberia and the Bering Sea (Figure 3a). A similar
188 dipole structure is evident in $V'T'_{850}$: negative anomalies extend zonally along the southern flank of the climatological heat
189 flux maximum, with the reduction more pronounced over the downstream region of the storm track. Concurrently, prominent
190 positive anomalies cover eastern Siberia, the Kamchatka Peninsula, and Alaska (Figure 3b), indicating enhanced poleward
191 eddy heat transport driven by East Asian dust outflow. These results suggest that increased springtime East Asian dust loading
192 is associated with a poleward shift of the North Pacific storm track and a strengthening of poleward eddy heat transport on
193 interannual timescales. The precipitation response corroborates this poleward shift, with reduced rainfall along the southern
194 flank and a slight enhancement near the Bering Sea (Figure S2).



195

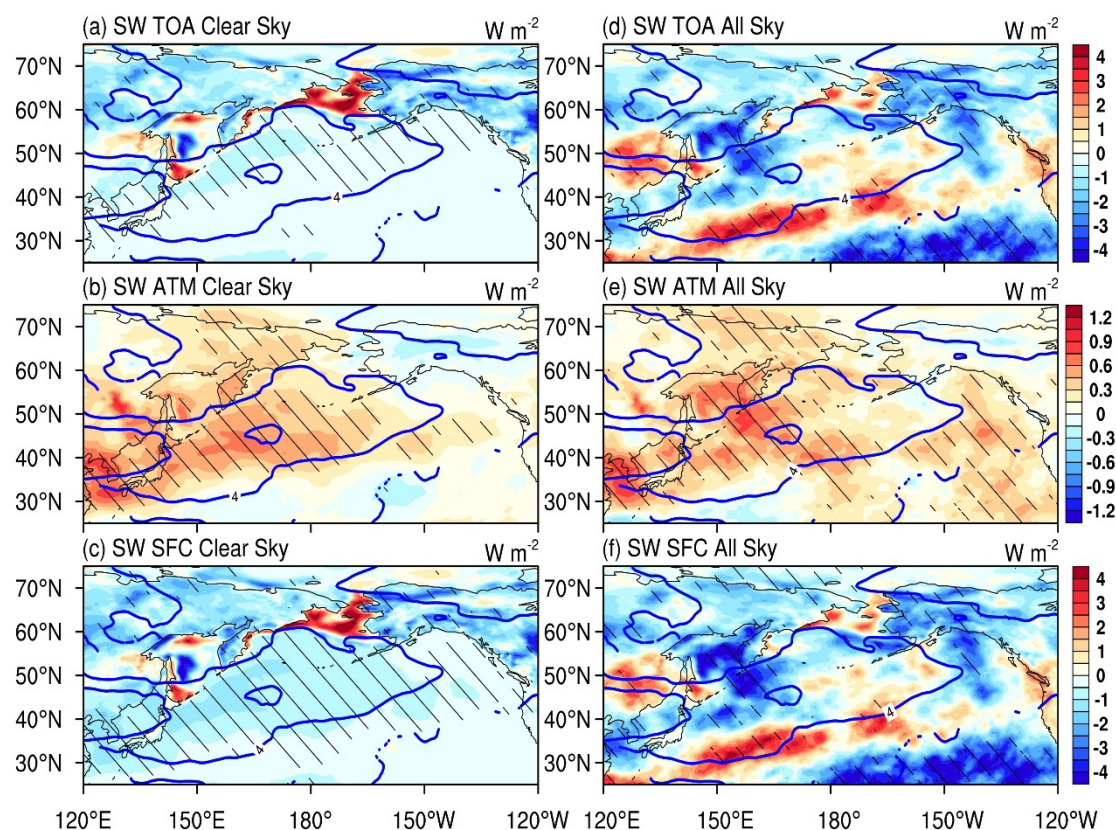
196 **Figure 3. Regressions of anomalies in (a) transient variances of 300 hPa geopotential height ($Z'Z'_{300}$; shading; dagpm²) and (b)**
 197 **850 hPa transient eddy meridional heat flux ($V'T'_{850}$; shading; K m s⁻¹) onto the standardized EADI_IA. Grey contours denote the**
 198 **climatological spring mean of (a) $Z'Z'_{300}$ and (b) $V'T'_{850}$. Hatching denotes the anomalies statistically significant at the 95%**
 199 **confidence level based on the Student's t test.**

200 3.2 Possible physical mechanism underlying the dust aerosol–storm tracks relationship

201 Having established the statistical association between East Asian dust loading and the poleward shift of the North Pacific storm
 202 track, we then examine the possible underlying physical mechanisms. Given dust aerosols perturb the radiative energy balance
 203 through scattering and absorbing solar radiation, thereby redistributing radiative energy, and modifying the large-scale
 204 circulation, we first examine the shortwave (SW) radiative flux anomalies associated with East Asian dust loading (Figure 4).
 205 Under clear-sky conditions (Figure 4a–c), dust aerosols transported over the North Pacific backscatters a fraction of incoming
 206 solar radiation, reducing the net downward SW flux at the top of the atmosphere (TOA) by approximately 1 W m⁻² over the
 207 dust polluted region (Figure 4a). Simultaneously, absorption of solar radiation by mineral dust induces a significant positive



208 radiative forcing of $0.3\text{--}0.6\text{ W m}^{-2}$ in the atmosphere (Figure 4b), leading to direct heating the atmospheric column. The
 209 combined effects of scattering and atmospheric absorption generate a pronounced dimming effect at the ground surface,
 210 reducing the net SW flux by $1.0\text{--}1.5\text{ W m}^{-2}$ over regions with high dust loading (Figure 4c). These magnitudes of dust-induced
 211 SW radiative perturbations are broadly consistent with previous estimates over the North Pacific (Zhu et al., 2007; Hu et al.,
 212 2019).



213
 214 **Figure 4. Regressions of anomalies in shortwave radiative fluxes (shading; W m^{-2}) at (a, d) the top of the atmosphere (TOA), (b, e)**
 215 **in the atmosphere (ATM), and (c, f) at the surface (SFC) and dust column mass density (blue contour with interval of 2 mg m^{-2})**
 216 **onto the standardized EADI_IA. The left column (a, b, c) represents clear-sky conditions, and the right column (d, e, f) represents**
 217 **all-sky conditions. Downward radiation is defined as positive at the TOA and the SFC; therefore, positive (negative) value means**
 218 **absorb/warming (irradiate/cooling) effects in the ATM. Hatching indicates that the regressed anomalies in shortwave radiative**
 219 **fluxes are statistically significant at the 95 % confidence level based on a Student's t test.**

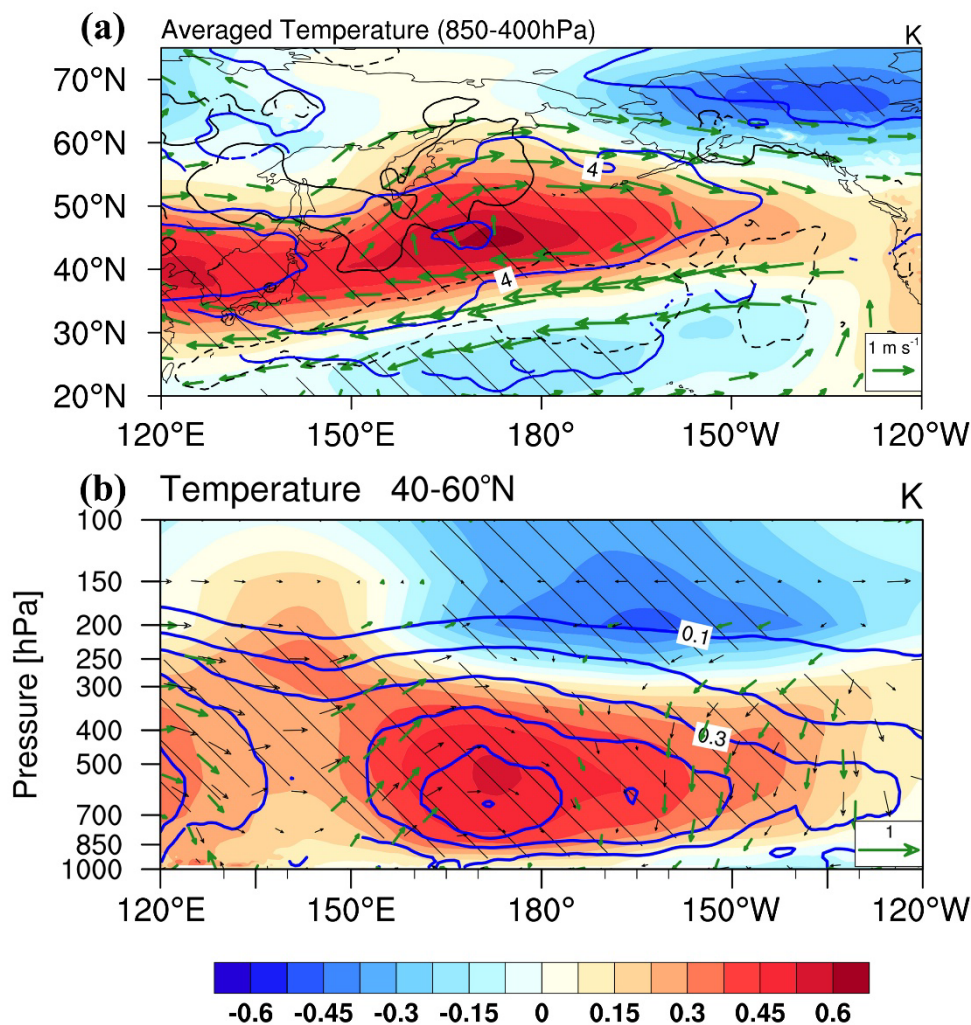
220 Under all-sky conditions (Figure 4d–f), cloud cover substantially modulates these radiative effects. Over the Sea of Okhotsk
 221 and the region south of the Kuril Islands, increased cloudiness (consistent with the enhanced precipitation shown in Figure S2)
 222 reflects additional solar radiation, amplifying the negative TOA forcing relative to clear-sky conditions (Figure 4d).
 223 Furthermore, when dust resides above cloud layers, the underlying clouds provide as a bright reflective surface that enhances
 224 the multiple scattering between the aerosol and cloud layers, thereby amplifying both the atmospheric absorption and the



225 surface cooling effects (Figure 4e–f). This amplification phenomenon is consistent with the satellite-based analysis of Xu et
226 al. (2017).

227

228 The enhanced shortwave absorption documented above is expected to warm the mid-troposphere and subsequently modify the
229 large-scale circulation. Figure 5a shows the 850–400 hPa averaged temperature and 500 hPa wind anomalies regressed onto
230 the interannual EADI. A zonally elongated band of significant positive temperature anomalies extends from East Asia across
231 the North Pacific between approximately 30°N and 60°N, closely matching the spatial distribution of the dust plume. The
232 warming maximum exceeds 0.6 K over the central North Pacific near 45°N, 170°E, where dust loading is most concentrated.
233 This spatial collocation strongly suggests that the mid-tropospheric warming is largely induced by dust aerosol absorption. In
234 response to this robust diabatic heating, the atmospheric column expands, thereby exciting an anomalous high-pressure system.
235 This thermodynamic adjustment is clearly characterized by a large-scale anticyclonic circulation anomaly in the 500 hPa wind
236 field over the North Pacific basin. Furthermore, the anomalous southerly winds near 165°E (Figure 5a), embedded within the
237 western flank of this anticyclone, may advect warmer subtropical air poleward, providing a supplementary positive temperature
238 tendency.



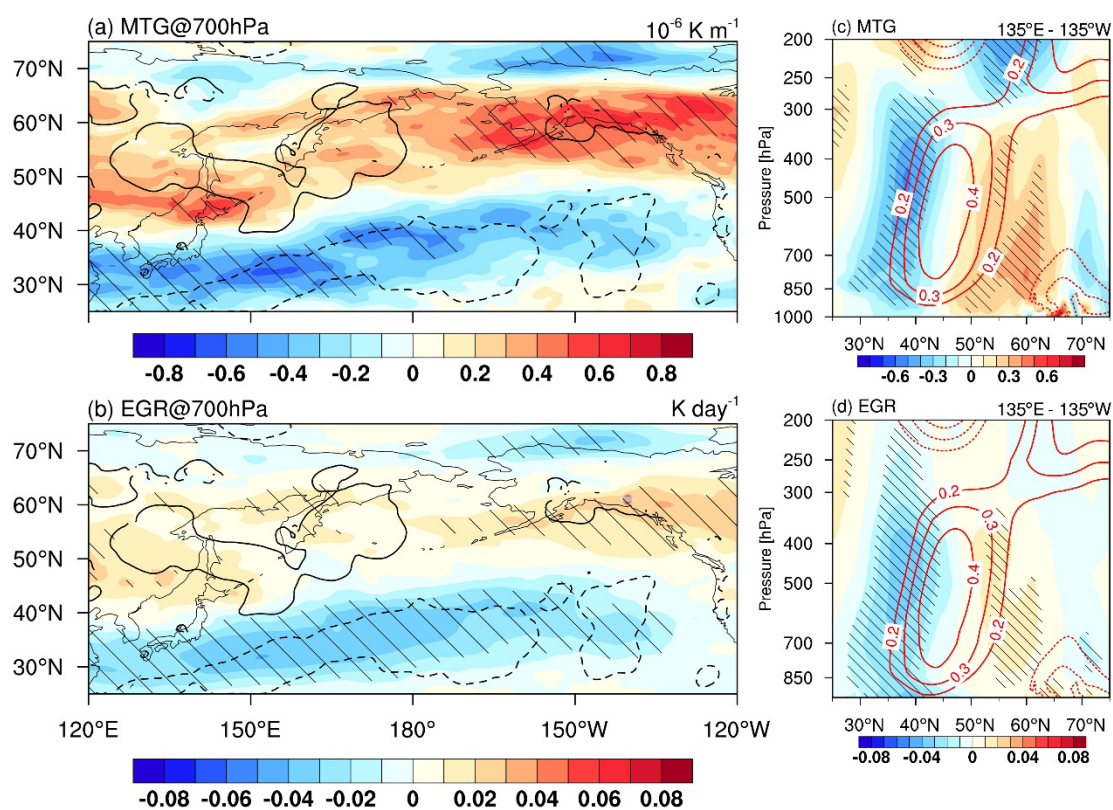
239

240 **Figure 5. (a) Regressions of anomalies in averaged temperature between 850 and 400 hPa (shading; K), 500 hPa wind (vector; m s⁻¹),**
 241 **and dust column mass density (blue contours with an interval of 2 mg m⁻²) onto the standardized EADI_1A. (b) Pressure-longitude**
 242 **cross section of the regressed anomalies in temperature (shading; K), zonal and vertical winds (vectors), and dust mass concentration**
 243 **(blue contours with an interval of 0.1 $\mu\text{g m}^{-3}$) averaged over the latitudinal band of 40° to 60°N. Black contours in (a) denote the**
 244 **statistically significant regions of the regressed $V'T'_{850}$ anomalies shown in Figure 3b. Hatching and green vectors indicate that the**
 245 **regressed anomalies in temperature and wind are statistically significant at the 95 % confidence level based on a Student's t test,**
 246 **respectively.**

247 The vertical structure of the temperature response is further examined in Figure 5b, which shows the regression of meridionally
 248 averaged (40°–60°N) temperature and dust mass concentration anomalies onto the interannual EADI. The eastward-
 249 transported dust plume is primarily confined below 300 hPa level. This vertical distribution aligns well with previous satellite-
 250 based studies of individual trans-Pacific dust transport events (Guo et al., 2017; Voss and Evan, 2020). Correspondingly, the
 251 dust-induced atmospheric heating is highly concentrated in the middle and lower troposphere. A significant warm layer is
 252 collocated with the dust mass concentration anomalies, featuring a maximum warming center between 850 and 400 hPa.



253 Beyond direct shortwave absorption, large-scale dynamical feedbacks may further reinforce this mid-tropospheric warming.
 254 The anomalous anticyclonic circulation established over the central North Pacific (Figure 5a) is associated with subsidence to
 255 its east (east of $\sim 180^\circ\text{E}$, Figure 5b), which likely contributes additional adiabatic warming through descending motion.
 256
 257 The dust-induced mid-tropospheric warming is concentrated in a zonal band over the central North Pacific (Figure 5a), which
 258 is expected to modify the meridional temperature gradient (MTG) and, through thermal wind balance, the atmospheric
 259 baroclinicity. As shown in Figure 6a, the 700 hPa MTG significantly increases along the northern flank of the North Pacific
 260 and decreases on the southern flank. This dipole pattern is a thermodynamically consistent consequence of the localized dust
 261 heating center identified above. The vertical cross-section averaged between 135°E and 135°W (Figure 6c) further confirms
 262 this structure, revealing a robust positive MTG anomaly north of 45°N and a negative anomaly to the south. These MTG
 263 anomalies are closely collocated with the northern and southern boundaries of the dust-induced warming center.



264
 265 **Figure 6. Regressions of anomalies in (a) the 700 hPa meridional temperature gradient (MTG; shading; 10^{-6} K m^{-1}) and (b) the 700**
 266 **hPa maximum Eady growth rate (EGR; shading; K day^{-1}) onto the standardized EADI_IA. Panels (c) and (d) display the meridional**
 267 **vertical cross sections of the regressed (c) MTG and (d) EGR anomalies averaged from 135°E to 135°W . Black contours in (a) and**
 268 **(b) denote the statistically significant regions of the regressed $V'T'_{850}$ anomalies shown in Figure 3b. Red contours in (c) and (d)**
 269 **represent the regressed temperature anomalies (K), with solid and dashed lines indicating positive and negative values, respectively.**
 270 **Hatching indicates that the regressed MTG and EGR anomalies are statistically significant at the 95 % confidence level based on a**
 271 **Student's t test.**



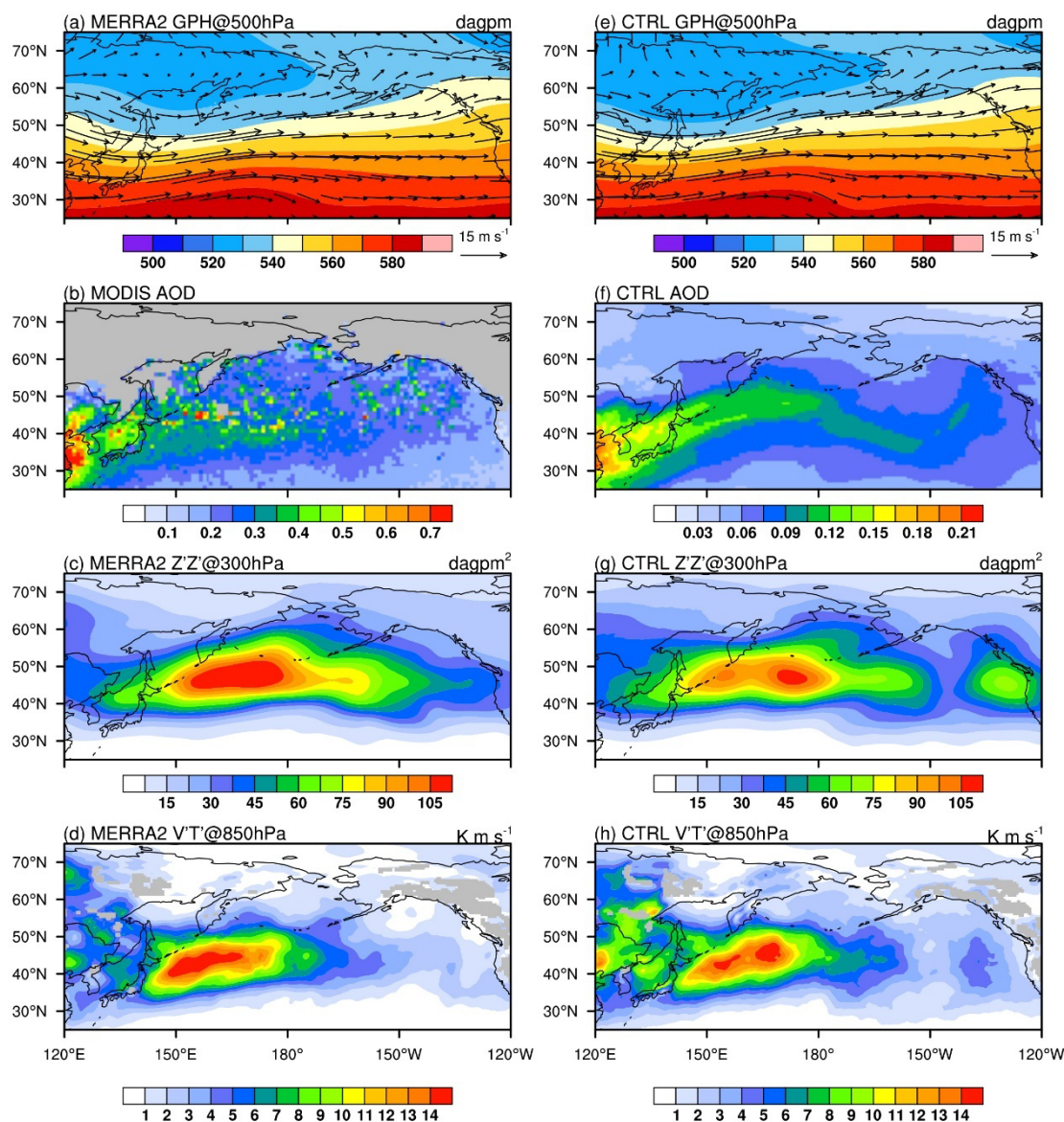
272 Because baroclinic instability is fundamentally governed by the MTG, the EGR exhibits an almost identical spatial response
273 (Lindzen and Farrell, 1980; Simmonds and Lim, 2009). At 700 hPa (Figure 6b), the baroclinicity strengthens in the north and
274 weakens in the south. The vertical profile of the EGR anomalies (Figure 6d) closely mirrors that of the MTG throughout the
275 lower and middle troposphere. Importantly, the spatial distribution of these EGR anomalies matches the regions of significant
276 storm track changes, indicating that the baroclinic adjustment directly shapes the optimal zone for transient eddy growth
277 (Chang and Lee and Swanson, 2002).

278

279 The preceding observational analysis outlines a consistent physical pathway for the dust effect on the North Pacific storm track.
280 Springtime East Asian dust absorbs shortwave radiation, warming the mid-troposphere. This heating restructures the
281 meridional temperature gradient and alters atmospheric baroclinicity. As a result, the favorable zone for baroclinic eddy growth
282 shifts to higher latitudes. To further to explicitly investigate and quantify this physical mechanism, we therefore employ targeted
283 numerical simulations in the next section

284 3.3 Quantitative analysis on the effect of dust radiative forcing

285 To isolate the causal role of the storm track response to dust radiative forcing, we conduct two sets of WRF-Chem ensemble
286 simulations for the spring of 2018. Before examining the specific aerosol effects, we evaluate the baseline model performance.
287 Figure 7 compares the spatial patterns of key variables between the observations (MERRA-2 and MODIS) and the CTRL
288 simulation. The CTRL experiment reasonably reproduces the spring mid-tropospheric circulation, including the East Asian
289 trough and the westerly stream at 500 hPa (Figures 7a and 7e). For AOD, the simulated magnitude is naturally lower than the
290 MODIS total aerosol retrievals because the CTRL run includes only dust emissions. This simulated magnitude nevertheless
291 remains quantitatively comparable to the observed dust AOD (Voss and Evan, 2020). The model also successfully captures
292 the spatial distribution and the trans-Pacific transport pathway of the dust plume (Figures 7b and 7f). Furthermore, the spatial
293 patterns of both the upper-tropospheric ($Z'Z'_{300}$) and lower-tropospheric ($V'T'_{850}$) storm track metrics are reasonably well
294 captured (Figures 7c, 7d, 7g, and 7h). These results demonstrate that the WRF-Chem model is suitable for investigating the
295 subsequent interactions between dust aerosols and the storm track.



296

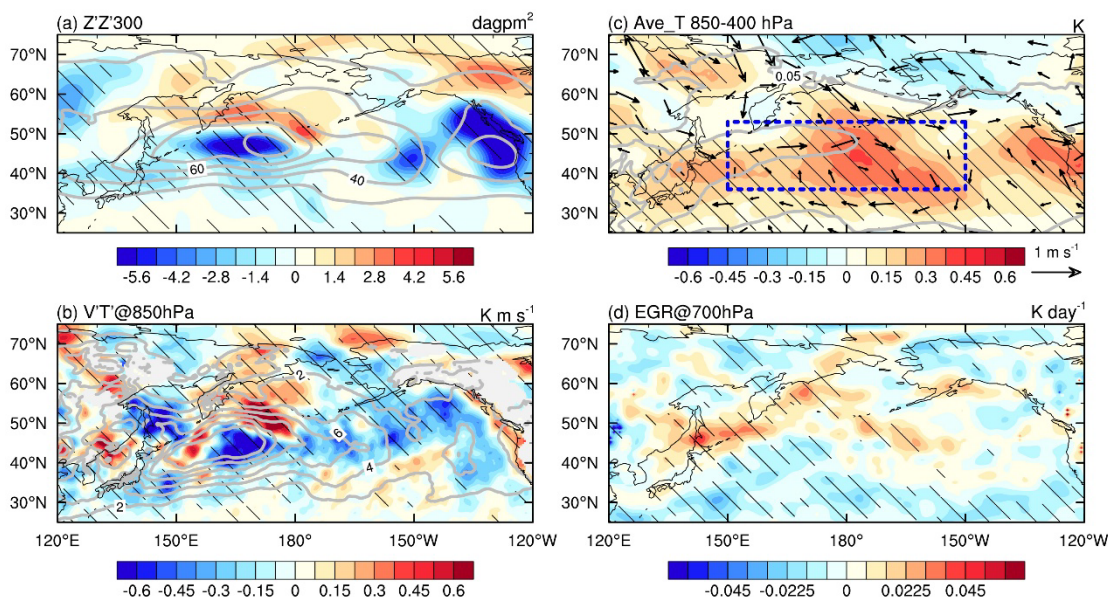
297 **Figure 7. Spatial distributions of (a, e) 500 hPa geopotential height (shading; dagpm) and wind (vectors; m s⁻¹), (b, f) aerosol optical**
 298 **depth (AOD; shading; unitless), (c, g) Z'Z'300 (shading; dagpm²), and (d, h) V'T'850 (shading; K m s⁻¹) averaged over spring (MAM)**
 299 **of 2018. The left column (a, b, c, d) represents the observational and reanalysis data (MERRA-2 for meteorological fields and MODIS**
 300 **for AOD). The right column (e, f, g, h) shows the corresponding ensemble mean of the WRF-Chem CTRL experiment.**

301

302 The model results corroborate the physical mechanism inferred from the observational analysis, reproducing both the spatial
 303 pattern and the sign of the storm track anomalies. As shown in Figure 8c, the dust radiative forcing induces a pronounced
 304 warming in the mid-troposphere (850 to 400 hPa) over the North Pacific, accompanied by an anomalous anticyclonic
 305 circulation at 500 hPa. The spatial pattern of this warming aligns well with the simulated dust AOD. This localized heating
 306 alters the environmental thermal field, thereby modifying the atmospheric baroclinicity. Consequently, the EGR at 700 hPa



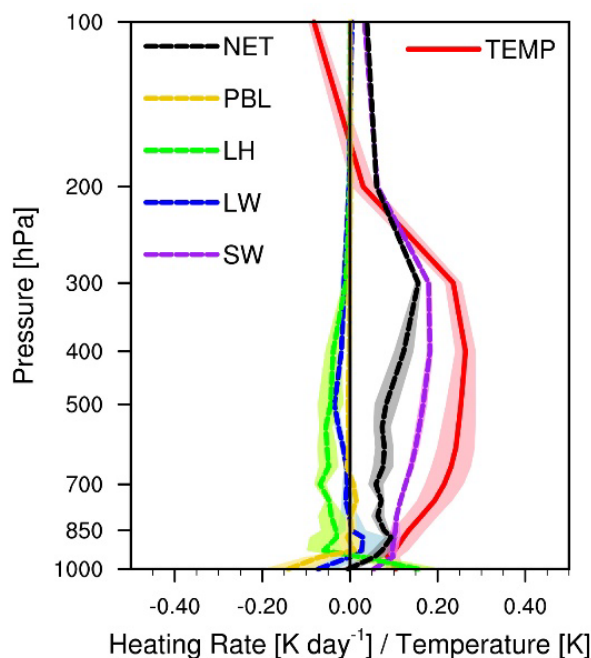
307 increases on the northern flank of the climatological storm track and decreases on the southern flank (Figure 8d). In response
 308 to these changes in baroclinic instability, both the upper-tropospheric ($Z'Z'_{300}$) and lower-tropospheric ($V'T'_{850}$) storm track
 309 metrics exhibit a clear poleward displacement (Figures 8a and 8b). Ultimately, the WRF-Chem sensitivity experiments provide
 310 causal evidence that dust-induced radiative heating shifts the North Pacific storm track poleward.



311

312 **Figure 8.** Differences (CTRL minus NoDust) in (a) $Z'Z'_{300}$ (shading; dagm^2), and (b) $V'T'_{850}$ (shading; K m s^{-1}), (c) averaged
 313 temperature between 850 and 400 hPa (shading; K), 500 hPa wind (vectors; m s^{-1}), and AOD (grey contours), and (d) 700 hPa EGR
 314 (shading; K day^{-1}). Grey contours in (a) and (b) represent the corresponding values in the CTRL experiment. Hatching indicates
 315 that the differences are statistically significant at the 95 % confidence level based on a Student's t test.

316 To further examine the physical processes responsible for the mid-tropospheric warming shown in Figure 8c, Figure 9 presents
 317 the vertical profiles of temperature and atmospheric heating rate differences (CTRL minus NoDust) averaged over the main
 318 warming region in the North Pacific (150°E to 150°W , 35° to 53°N ; blue dashed box in Figure 8c). The temperature profile
 319 shows a pronounced warming throughout the troposphere below 200 hPa, with a slight cooling above this level. This vertical
 320 structure is consistent with the observational regression results shown in Figure 5b. Among the contributing heating processes,
 321 shortwave radiation is the sole positive heating term, with its maximum at near 400 hPa. Longwave radiation and latent heating
 322 both make modest negative contributions throughout the column. As a result, the net heating profile closely follows the
 323 shortwave radiative heating, confirming that the dust-induced atmospheric warming is primarily driven by shortwave
 324 absorption.

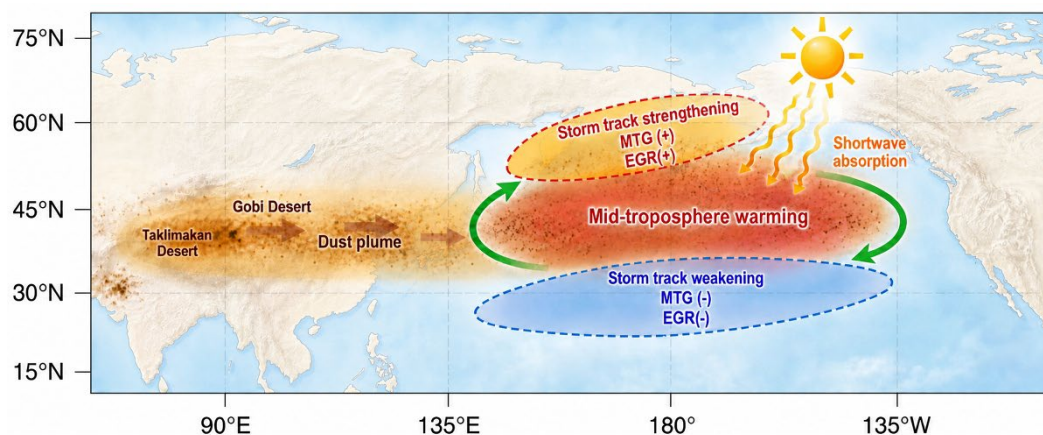


325

326 **Figure 9.** Vertical profiles of differences (CTRL minus NoDust) in temperature (solid red line; K) and atmospheric heating rates
327 (dashed line; K d^{-1}) averaged over the North Pacific (150°E – 150°W , 35 – 53°N , as outlined in Figure 8c). Here, atmospheric heating
328 rates include shortwave (SW) and longwave (LW) radiation heating, latent heating (LH, i.e., heating from the microphysics and
329 cumulus scheme), and heating from the planetary boundary layer (PBL) scheme. Net heating rate (NET) = SW + LW + LH + PBL.

330 4 Conclusions and discussion

331 This study demonstrates that springtime East Asian dust aerosols exert a systematic poleward influence on the North Pacific
332 storm track on interannual timescales. Using MERRA-2 reanalysis data spanning 1980–2022, we identify a statistically robust
333 association between anomalously high East Asian dust loading and a meridional dipole pattern in storm track activity,
334 characterized by weakening on the equatorward flank and strengthening on the poleward flank. The underlying mechanism
335 follows a coherent physical pathway (Figure 10). Specifically, shortwave absorption by the trans-Pacific dust plume heats the
336 mid-troposphere (850–400 hPa), which excites an anomalous anticyclonic circulation. This circulation restructures the
337 meridional temperature gradient into a north-positive/south-negative dipole pattern, and consequently shifts the zone of
338 maximum Eady growth rate poleward, favoring baroclinic eddy development at higher latitudes. Model sensitivity experiments
339 for spring 2018 reproduce both the spatial pattern and the sign of this response, confirming that dust shortwave absorption is
340 sufficient to drive the observed poleward displacement of the storm track.



341

342 **Figure 10. Schematic diagram illustrating the physical mechanism by which springtime East Asian dust aerosols drive a poleward**
 343 **shift of the North Pacific storm track. Dust emitted from East Asian sources is transported eastward across the North Pacific by**
 344 **mid-latitude westerlies. Shortwave absorption by the dust plume warms the mid-troposphere, enhancing (reducing) the meridional**
 345 **temperature gradient (MTG) on the poleward (equatorward) flank. The resulting dipole in the maximum Eady growth rate (EGR)**
 346 **favours storm track strengthening at higher latitudes and weakening at lower latitudes, producing a net poleward displacement.**

347 It is important to distinguish the effects of dust aerosols from those of anthropogenic aerosols on the North Pacific storm track.
 348 Previous studies have shown that East Asian anthropogenic emissions predominantly intensify the storm track through aerosol-
 349 cloud interactions and associated latent heat release (Wang et al., 2014; Zhang et al., 2007). In contrast, our findings highlight
 350 that dust aerosols mainly alter the latitudinal position of the storm track via aerosol-radiation interactions. This distinct response
 351 is driven by the direct radiative heating of the dust layer. Furthermore, mid-latitude transient eddies play a critical role in the
 352 poleward transport of heat, moisture, and momentum (Shaw et al., 2016; Tamarin-Brodsky and Kaspi, 2017; Hoskins and
 353 Hodges, 2019). The dust-induced poleward shift, particularly the enhanced transient meridional heat flux near the Bering Sea
 354 (Figure 3b), may substantially accelerate springtime Arctic-sea ice melting and trigger subsequent climate feedbacks (Overland
 355 and Pease, 1982; Huang et al., 2019; Peng et al., 2021). These potential impacts warrant further investigation.

356

357 It is worth noting that the WRF-Chem simulated responses in both temperature and storm track metrics are weaker than those
 358 inferred from the observational regression analysis. Several factors may contribute to this discrepancy. First, the dust loading
 359 over East Asia and the North Pacific originates not only from local East Asian sources but also from long-range transport from
 360 the Middle East and North Africa (Creamean et al., 2013; Hu et al., 2019; Zhou et al., 2024; Huang et al., 2025). Our regional
 361 model domain does not fully capture these remote contributions, which would lead to an underestimation of the total dust
 362 burden and the associated radiative heating over the North Pacific. Second, the shortwave absorptive capacity of dust is likely
 363 underestimated in our simulations. Observational studies have shown that East Asian dust readily mixes with anthropogenic
 364 aerosol species during long-range transport, and such internally mixed dust aerosols can be more than 50% more absorbing
 365 than pure dust (Tian et al., 2018). Since our WRF-Chem experiments excluded anthropogenic emissions by design, this
 366 absorption enhancement associated with mixing was not represented. Third, the four-band shortwave radiation scheme used



367 in our WRF-Chem configuration tends to underestimate dust shortwave heating rates relative to schemes with finer spectral
368 resolution (Feng et al., 2025), which would further weaken the simulated thermal response. Nevertheless, the primary purpose
369 of the WRF-Chem experiments in this study is to provide a process-level verification of the physical mechanism identified
370 from the observational analysis, rather than to achieve precise quantitative agreement.

371

372 Beyond direct radiative heating, dust particles can also act as ice nucleating particles and alter the atmospheric energy budget
373 through aerosol-cloud interactions (Uno et al., 2009; Zeng et al., 2023; Chen et al., 2024). Our current model configuration
374 did not account for these indirect microphysical effects. Therefore, achieving a more precise quantitative assessment of the
375 storm track response will require future studies to incorporate refined dust optical properties, realistic aerosol mixing
376 representations, and these complex aerosol-cloud interactions.

377 **Code and data availability**

378 The source codes of WRF-Chem model are available at https://www2.mmm.ucar.edu/wrf/users/download/get_source.html
379 (UCAR, 2022). The FNL data are available at <https://rda.ucar.edu/datasets/ds083.2/> (Ncep, 2000). MERRA-2 reanalysis data
380 are available at <https://disc.gsfc.nasa.gov/datasets> (GMAO, 2015). The MODIS AOD are available at
381 https://ladsweb.modaps.eosdis.nasa.gov/missions-and-measurements/products/MOD08_M3 (Platnick, et al., 2015). CMAP
382 precipitation are available at <https://disc.gsfc.nasa.gov/datasets> (Xie and Arkin, 1997).

383 **Author contributions**

384 XH, HX and AZ conceptualized the research goals and developed the methodology, including the experimental setup. AZ
385 carried out the investigation, performed the formal analysis, and visualized the results. JD and AD also contributed to the
386 supervision of the work. LX, ZW, KD and TL contributed to data curation. AZ prepared the manuscript with contributions
387 from all co-authors, and all authors contributed to the writing (review and editing) of the final article.

388 **Competing interests**

389 The contact author has declared that none of the authors has any competing interests.

390 **Acknowledgements**

391 We are grateful to the High Performance Computing Center (HPCC) of Nanjing University for doing the numerical calculations
392 in this paper on its blade cluster system. We also thank all the corresponding institutions for providing their data for this study.
393 Additionally, we acknowledge the use of the GPT image 2 model (OpenAI) for the visual optimization of the schematic



394 diagram presented in Figure 10, while emphasizing that the scientific concepts and physical mechanisms depicted therein
395 remain entirely the work of the authors.

396 **Financial support**

397 This work was supported by the National Natural Science Foundation of China (42588101) and the New Cornerstone Science
398 Foundation through the XPLOER PRIZE.

399 **Review statement**

400 **References**

- 401 Awan, J. A. and Bae, D.-H.: Features and interdecadal variability of droughts in the homogeneous rainfall zones over the East
402 Asian monsoon region, *Int. J. Climatol.*, 36, 1943–1953, <https://doi.org/10.1002/joc.4471>, 2016.
- 403 Bao, Z., Wen, Z., and Wu, R.: Variability of aerosol optical depth over east Asia and its possible impacts, *J. Geophys. Res.-*
404 *Atmos.*, 114, D14214, <https://doi.org/10.1029/2008JD010603>, 2009.
- 405 Bender, F. A.-M., Ramanathan, V., and Tselioudis, G.: Changes in extratropical storm track cloudiness 1983–2008:
406 observational support for a poleward shift, *Clim. Dynam.*, 38, 2037–2053, <https://doi.org/10.1007/s00382-011-1065-6>, 2012.
- 407 Blackmon, M. L.: A Climatological Spectral Study of the 500 mb Geopotential Height of the Northern Hemisphere, *J. Atmos.*
408 *Sci.*, 33, 1607–1623, [https://doi.org/10.1175/1520-0469\(1976\)033<1607:ACSSOT>2.0.CO;2](https://doi.org/10.1175/1520-0469(1976)033<1607:ACSSOT>2.0.CO;2), 1976.
- 409 Bohren, C. F. and Huffman, D. R.: *Absorption and Scattering of Light by Small Particles*, John Wiley & Sons, New York,
410 USA, 1983.
- 411 Cai, W., van Rensch, P., Cowan, T., and Hendon, H. H.: Teleconnection Pathways of ENSO and the IOD and the Mechanisms
412 for Impacts on Australian Rainfall, *J. Climate*, 24, 3910–3923, <https://doi.org/10.1175/2011JCLI4129.1>, 2011.
- 413 Chang, E. K. M., Lee, S., and Swanson, K. L.: Storm Track Dynamics, *J. Climate*, 15, 2163–2183,
414 [https://doi.org/10.1175/1520-0442\(2002\)015<2163:STD>2.0.CO;2](https://doi.org/10.1175/1520-0442(2002)015<2163:STD>2.0.CO;2), 2002.
- 415 Chemke, R. and Yuval, J.: Climate change shifts the North Pacific storm track polewards, *Nature*, 649, 626–630,
416 <https://doi.org/10.1038/s41586-025-09895-y>, 2026.
- 417 Chen, J., Xu, J., Wu, Z., Meng, X., Yu, Y., Ginoux, P., DeMott, P. J., Xu, R., Zhai, L., Yan, Y., Zhao, C., Li, S.-M., Zhu, T.,
418 and Hu, M.: Decreased dust particles amplify the cloud cooling effect by regulating cloud ice formation over the Tibetan
419 Plateau, *Sci. Adv.*, 10, eado0885, <https://doi.org/10.1126/sciadv.ado0885>, 2024.
- 420 Chen, S., Huang, J., Qian, Y., Zhao, C., Kang, L., Yang, B., Wang, Y., Liu, Y., Yuan, T., Wang, T., Ma, X., and Zhang, G.:
421 An overview of mineral dust modeling over East Asia, *J. Meteorol. Res.*, 31, 633–653, <https://doi.org/10.1007/s13351-017->
422 6142-2, 2017.



- 423 Chen, Y., Yang, K., Zhou, D., Qin, J., and Guo, X.: Improving the Noah Land Surface Model in Arid Regions with an
424 Appropriate Parameterization of the Thermal Roughness Length, *J. Hydrometeorol.*, 11, 995–1006,
425 <https://doi.org/10.1175/2010JHM1185.1>, 2010.
- 426 Chen, Y., Chen, S., Zhou, J., Zhao, D., Bi, H., Zhang, Y., Alam, K., Yu, H., Yang, Y., and Chen, J.: A super dust storm
427 enhanced by radiative feedback, *npj Clim. Atmos. Sci.*, 6, 90, <https://doi.org/10.1038/s41612-023-00418-y>, 2023.
- 428 Chin, M., Ginoux, P., Kinne, S., Torres, O., Holben, B. N., Duncan, B. N., Martin, R. V., Logan, J. A., Higurashi, A., and
429 Nakajima, T.: Tropospheric Aerosol Optical Thickness from the GOCART Model and Comparisons with Satellite and Sun
430 Photometer Measurements, *J. Atmos. Sci.*, 59, 461–483, [https://doi.org/10.1175/1520-0469\(2002\)059<0461:TAOTFT>2.0.CO;2](https://doi.org/10.1175/1520-0469(2002)059<0461:TAOTFT>2.0.CO;2), 2002.
- 432 Creamean, J. M., Suski, K. J., Rosenfeld, D., Cazorla, A., DeMott, P. J., Sullivan, R. C., White, A. B., Ralph, F. M., Minnis,
433 P., Comstock, J. M., Tomlinson, J. M., and Prather, K. A.: Dust and Biological Aerosols from the Sahara and Asia Influence
434 Precipitation in the Western U.S., *Science*, 339, 1572–1578, <https://doi.org/10.1126/science.1227279>, 2013.
- 435 Feng, J., Zhao, C., Du, Q., Yang, Z., and Jin, C.: Amending the algorithm of aerosol–radiation interactions in WRF-Chem
436 (v4.4), *Geosci. Model Dev.*, 18, 585–603, <https://doi.org/10.5194/gmd-18-585-2025>, 2025.
- 437 Fu, Y., Wu, C., Gao, S., Peñuelas, J., Camarero, J. J., Zhang, J., Li, D., Zheng, X., Li, Z., Wang, Y., Liang, E., and Piao, S.:
438 Vegetation greening drives long-term dust mitigation in Eastern Asia, *Nat. Commun.*, 17, 1729,
439 <https://doi.org/10.1038/s41467-026-68427-y>, 2026.
- 440 Gelaro, R., McCarty, W., Suárez, M. J., Todling, R., Molod, A., Takacs, L., Randles, C. A., Darmenov, A., Bosilovich, M. G.,
441 Reichle, R., Wargan, K., Coy, L., Cullather, R., Draper, C., Akella, S., Buchard, V., Conaty, A., da Silva, A. M., Gu, W., Kim,
442 G.-K., Koster, R., Lucchesi, R., Merkova, D., Nielsen, J. E., Partyka, G., Pawson, S., Putman, W., Rienecker, M., Schubert, S.
443 D., Sienkiewicz, M., and Zhao, B.: The Modern-Era Retrospective Analysis for Research and Applications, Version 2
444 (MERRA-2), *J. Climate*, 30, 5419–5454, <https://doi.org/10.1175/JCLI-D-16-0758.1>, 2017.
- 445 Global Modeling and Assimilation Office (GMAO): MERRA-2 instM_3d_asm_Np: 3d, Monthly mean, Instantaneous,
446 Pressure-Level, Assimilation, Assimilated Meteorological Fields V5.12.4, Goddard Earth Sciences Data and Information
447 Services Center (GES DISC) [data set], <https://doi.org/10.5067/2E096JV59PK7>, 2015.
- 448 Grell, G. A.: Prognostic Evaluation of Assumptions Used by Cumulus Parameterizations, *Mon. Weather Rev.*, 121, 764–787,
449 [https://doi.org/10.1175/1520-0493\(1993\)121<0764:PEOAUB>2.0.CO;2](https://doi.org/10.1175/1520-0493(1993)121<0764:PEOAUB>2.0.CO;2), 1993.
- 450 Grell, G. A. and Dévényi, D.: A generalized approach to parameterizing convection combining ensemble and data assimilation
451 techniques, *Geophys. Res. Lett.*, 29, 38-1–38-4, <https://doi.org/10.1029/2002GL015311>, 2002.
- 452 Gui, K., Yao, W., Che, H., An, L., Zheng, Y., Li, L., Zhao, H., Zhang, L., Zhong, J., Wang, Y., and Zhang, X.: Record-breaking
453 dust loading during two mega dust storm events over northern China in March 2021: aerosol optical and radiative properties
454 and meteorological drivers, *Atmos. Chem. Phys.*, 22, 7905–7932, <https://doi.org/10.5194/acp-22-7905-2022>, 2022.



- 455 Guo, J., Xu, H., Liu, L., Chen, D., Peng, Y., Yim, S. H.-L., Yang, Y., Li, J., Zhao, C., and Zhai, P.: The Trend Reversal of
456 Dust Aerosol Over East Asia and the North Pacific Ocean Attributed to Large-Scale Meteorology, Deposition, and Soil
457 Moisture, *J. Geophys. Res.-Atmos.*, 124, 10450–10466, <https://doi.org/10.1029/2019JD030654>, 2019.
- 458 Guo, J., Lou, M., Miao, Y., Wang, Y., Zeng, Z., Liu, H., He, J., Xu, H., Wang, F., Min, M., and Zhai, P.: Trans-Pacific transport
459 of dust aerosols from East Asia: Insights gained from multiple observations and modeling, *Environ. Pollut.*, 230, 1030–1039,
460 <https://doi.org/10.1016/j.envpol.2017.07.062>, 2017.
- 461 Gupta, P., Levy, R. C., Mattoo, S., Remer, L. A., and Munchak, L. A.: A surface reflectance scheme for retrieving aerosol
462 optical depth over urban surfaces in MODIS Dark Target retrieval algorithm, *Atmos. Meas. Tech.*, 9, 3293–3308,
463 <https://doi.org/10.5194/amt-9-3293-2016>, 2016.
- 464 Heidinger, A. K., Foster, M. J., Walther, A., and Zhao, X.: The Pathfinder Atmospheres–Extended AVHRR Climate Dataset,
465 *B. Am. Meteorol. Soc.*, 95, 909–922, <https://doi.org/10.1175/BAMS-D-12-00246.1>, 2014.
- 466 Holben, B. N., Eck, T. F., Slutsker, I., Tanré, D., Buis, J. P., Setzer, A., Vermote, E., Reagan, J. A., Kaufman, Y. J., Nakajima,
467 T., Lavenue, F., Jankowiak, I., and Smirnov, A.: AERONET—A Federated Instrument Network and Data Archive for Aerosol
468 Characterization, *Remote Sens. Environ.*, 66, 1–16, [https://doi.org/10.1016/S0034-4257\(98\)00031-5](https://doi.org/10.1016/S0034-4257(98)00031-5), 1998.
- 469 Hong, S.-Y., Noh, Y., and Dudhia, J.: A New Vertical Diffusion Package with an Explicit Treatment of Entrainment Processes,
470 *Mon. Weather Rev.*, 134, 2318–2341, <https://doi.org/10.1175/MWR3199.1>, 2006.
- 471 Hoskins, B. J. and Hodges, K. I.: The Annual Cycle of Northern Hemisphere Storm Tracks. Part I: Seasons, *J. Climate*, 32,
472 1743–1760, <https://doi.org/10.1175/JCLI-D-17-0870.1>, 2019.
- 473 Hu, Z., Huang, J., Zhao, C., Ma, Y., Jin, Q., Qian, Y., Leung, L. R., Bi, J., and Ma, J.: Trans-Pacific transport and evolution
474 of aerosols: spatiotemporal characteristics and source contributions, *Atmos. Chem. Phys.*, 19, 12709–12730,
475 <https://doi.org/10.5194/acp-19-12709-2019>, 2019.
- 476 Huang, J., Wang, T., Wang, W., Li, Z., and Yan, H.: Climate effects of dust aerosols over East Asian arid and semiarid regions,
477 *J. Geophys. Res.-Atmos.*, 119, 11398–11416, <https://doi.org/10.1002/2014JD021796>, 2014.
- 478 Huang, Y., Dong, X., Xi, B., and Deng, Y.: A survey of the atmospheric physical processes key to the onset of Arctic sea ice
479 melt in spring, *Clim. Dynam.*, 52, 4907–4922, <https://doi.org/10.1007/s00382-018-4422-x>, 2019.
- 480 Huang, Z., Liu, Q., Dong, Q., Hu, Z., Zhang, X., Li, Z., and Wang, Y.: Eastward Transport of African Dust and Its Climatic
481 and Environmental Impacts, *Adv. Earth Sci. (in Chinese)*, 40, 1–14, <https://doi.org/10.11867/j.issn.1001-8166.2025.004>, 2025.
- 482 Iacono, M. J., Delamere, J. S., Mlawer, E. J., Shephard, M. W., Clough, S. A., and Collins, W. D.: Radiative forcing by long-
483 lived greenhouse gases: Calculations with the AER radiative transfer models, *J. Geophys. Res.-Atmos.*, 113, D13103,
484 <https://doi.org/10.1029/2008JD009944>, 2008.
- 485 Idrissa, N. F., Zhao, C., Zhiyuan, H., Feng, J., and Du, Q.: Long-range transport impact of a severe dust storm over the Yangtze
486 River Basin region and its modeling sensitivity to dust emission scheme, *Atmos. Res.*, 310, 107612,
487 <https://doi.org/10.1016/j.atmosres.2024.107612>, 2024.



- 488 Jiang, T., Deng, Y., and Li, W.: Local kinetic energy budget of high-frequency and intermediate-frequency eddies: winter
489 climatology and interannual variability, *Clim. Dynam.*, 41, 961–976, <https://doi.org/10.1007/s00382-013-1684-1>, 2013.
- 490 Jin, Q., Wei, J., Lau, W. K. M., Pu, B., and Wang, C.: Interactions of Asian mineral dust with Indian summer monsoon: Recent
491 advances and challenges, *Earth-Sci. Rev.*, 215, 103562, <https://doi.org/10.1016/j.earscirev.2021.103562>, 2021.
- 492 Kahn, R. A., Gaitley, B. J., Martonchik, J. V., Diner, D. J., Crean, K. A., and Holben, B.: Multiangle Imaging
493 Spectroradiometer (MISR) global aerosol optical depth validation based on 2 years of coincident Aerosol Robotic Network
494 (AERONET) observations, *J. Geophys. Res.-Atmos.*, 110, D10S04, <https://doi.org/10.1029/2004JD004706>, 2005.
- 495 Kok, J. F., Storelvmo, T., Karydis, V. A., Adebisi, A. A., Mahowald, N. M., Evan, A. T., He, C., and Leung, D. M.: Mineral
496 dust aerosol impacts on global climate and climate change, *Nat. Rev. Earth Environ.*, 4, 71–86, <https://doi.org/10.1038/s43017-022-00379-5>, 2023.
- 498 Lau, K. M., Kim, M. K., and Kim, K. M.: Asian summer monsoon anomalies induced by aerosol direct forcing: the role of the
499 Tibetan Plateau, *Clim. Dynam.*, 26, 855–864, <https://doi.org/10.1007/s00382-006-0114-z>, 2006.
- 500 Levy, R. C., Remer, L. A., Kleidman, R. G., Mattoo, S., Ichoku, C., Kahn, R., and Eck, T. F.: Global evaluation of the
501 Collection 5 MODIS dark-target aerosol products over land, *Atmos. Chem. Phys.*, 10, 10399–10420,
502 <https://doi.org/10.5194/acp-10-10399-2010>, 2010.
- 503 Li, Y., Xu, F., Feng, J., Du, M., Song, W., Li, C., and Zhao, W.: Influence of the previous North Atlantic Oscillation (NAO)
504 on the spring dust aerosols over North China, *Atmos. Chem. Phys.*, 23, 6021–6042, <https://doi.org/10.5194/acp-23-6021-2023>,
505 2023.
- 506 Liguori, G., McGregor, S., Singh, M., Arblaster, J., and Di Lorenzo, E.: Revisiting ENSO and IOD Contributions to Australian
507 Precipitation, *Geophys. Res. Lett.*, 49, e2021GL094295, <https://doi.org/10.1029/2021GL094295>, 2022.
- 508 Lin, Y. and Colle, B. A.: A New Bulk Microphysical Scheme That Includes Riming Intensity and Temperature-Dependent Ice
509 Characteristics, *Mon. Weather Rev.*, 139, 1013–1035, <https://doi.org/10.1175/2010MWR3293.1>, 2011.
- 510 Lindzen, R. S. and Farrell, B.: A Simple Approximate Result for the Maximum Growth Rate of Baroclinic Instabilities, *J.*
511 *Atmos. Sci.*, 37, 1648–1654, [https://doi.org/10.1175/1520-0469\(1980\)037<1648:ASARFT>2.0.CO;2](https://doi.org/10.1175/1520-0469(1980)037<1648:ASARFT>2.0.CO;2), 1980.
- 512 Liu, Z., Ming, Y., Wang, L., Bollasina, M., Luo, M., Lau, N.-C., and Yim, S. H.-L.: A Model Investigation of Aerosol-Induced
513 Changes in the East Asian Winter Monsoon, *Geophys. Res. Lett.*, 46, 10186–10195, <https://doi.org/10.1029/2019GL084228>,
514 2019.
- 515 Ming, Y., Ramaswamy, V., and Chen, G.: A Model Investigation of Aerosol-Induced Changes in Boreal Winter Extratropical
516 Circulation, *J. Climate*, 24, 6077–6091, <https://doi.org/10.1175/2011JCLI4111.1>, 2011.
- 517 NCEP/National Weather Service/NOAA/U.S. Department of Commerce: NCEP FNL Operational Model Global Tropospheric
518 Analyses, continuing from July 1999, NSF National Center for Atmospheric Research [data set],
519 <https://doi.org/10.5065/D6M043C6>, 2000.
- 520 Overland, J. E. and Pease, C. H.: Cyclone Climatology of the Bering Sea and Its Relation to Sea Ice Extent, *Mon. Weather*
521 *Rev.*, 110, 5–13, [https://doi.org/10.1175/1520-0493\(1982\)110<0005:CCOTBS>2.0.CO;2](https://doi.org/10.1175/1520-0493(1982)110<0005:CCOTBS>2.0.CO;2), 1982.



- 522 Pahlow, M., Parlange, M. B., and Porté-Agel, F.: On Monin–Obukhov Similarity In The Stable Atmospheric Boundary Layer,
523 Bound.-Lay. Meteorol., 99, 225–248, <https://doi.org/10.1023/A:1018909000098>, 2001.
- 524 Peng, L., Zhang, X., Kim, J.-H., Cho, K.-H., Kim, B.-M., Wang, Z., and Tang, H.: Role of Intense Arctic Storm in Accelerating
525 Summer Sea Ice Melt: An In Situ Observational Study, Geophys. Res. Lett., 48, e2021GL092714,
526 <https://doi.org/10.1029/2021GL092714>, 2021.
- 527 Pfahl, S., Madonna, E., Boettcher, M., Joos, H., and Wernli, H.: Warm Conveyor Belts in the ERA-Interim Dataset (1979–
528 2010). Part II: Moisture Origin and Relevance for Precipitation, J. Climate, 27, 27–40, <https://doi.org/10.1175/JCLI-D-13-00223.1>, 2014.
- 530 Platnick, S., Meyer, K. G., King, M. D., Wind, G., Amarasinghe, N., Marchant, B., Arnold, G. T., Zhang, Z., Hubanks, P. A.,
531 Holz, R. E., Yang, P., Ridgway, W. L., and Riedi, J.: MODIS Atmosphere L3 Monthly Product (MOD08_M3), NASA MODIS
532 Adaptive Processing System, Goddard Space Flight Center [data set], https://doi.org/10.5067/MODIS/MOD08_M3.061, 2015.
- 533 Salathé Jr., E. P.: Influences of a shift in North Pacific storm tracks on western North American precipitation under global
534 warming, Geophys. Res. Lett., 33, L19820, <https://doi.org/10.1029/2006GL026882>, 2006.
- 535 Seager, R., Naik, N., Ting, M., Cane, M. A., Harnik, N., and Kushnir, Y.: Adjustment of the atmospheric circulation to tropical
536 Pacific SST anomalies: Variability of transient eddy propagation in the Pacific–North America sector, Q. J. Roy. Meteor. Soc.,
537 136, 277–296, <https://doi.org/10.1002/qj.588>, 2010.
- 538 Shao, Y.: Simplification of a dust emission scheme and comparison with data, J. Geophys. Res.-Atmos., 109, D10202,
539 <https://doi.org/10.1029/2003JD004372>, 2004.
- 540 Shaw, T. A., Baldwin, M., Barnes, E. A., Caballero, R., Garfinkel, C. I., Hwang, Y. T., Li, C., O’Gorman, P. A., Rivière, G.,
541 Simpson, I. R., and Voigt, A.: Storm track processes and the opposing influences of climate change, Nat. Geosci., 9, 656–664,
542 <https://doi.org/10.1038/ngeo2783>, 2016.
- 543 Simmonds, I. and Lim, E.-P.: Biases in the calculation of Southern Hemisphere mean baroclinic eddy growth rate, Geophys.
544 Res. Lett., 36, L01707, <https://doi.org/10.1029/2008GL036320>, 2009.
- 545 Simmons, A. J. and Hoskins, B. J.: The Life Cycles of Some Nonlinear Baroclinic Waves, J. Atmos. Sci., 35, 414–432,
546 [https://doi.org/10.1175/1520-0469\(1978\)035<0414:TLCOSN>2.0.CO;2](https://doi.org/10.1175/1520-0469(1978)035<0414:TLCOSN>2.0.CO;2), 1978.
- 547 Sokolik, I. N. and Toon, O. B.: Incorporation of mineralogical composition into models of the radiative properties of mineral
548 aerosol from UV to IR wavelengths, J. Geophys. Res.-Atmos., 104, 9423–9444, <https://doi.org/10.1029/1998JD200048>, 1999.
- 549 Stockwell, W. R., Middleton, P., Chang, J. S., and Tang, X.: The second generation regional acid deposition model chemical
550 mechanism for regional air quality modeling, J. Geophys. Res.-Atmos., 95, 16343–16367,
551 <https://doi.org/10.1029/JD095iD10p16343>, 1990.
- 552 Sun, Y. and Zhao, C.: Influence of Saharan Dust on the Large-Scale Meteorological Environment for Development of Tropical
553 Cyclone Over North Atlantic Ocean Basin, J. Geophys. Res.-Atmos., 125, e2020JD033454,
554 <https://doi.org/10.1029/2020JD033454>, 2020.



- 555 Tamarin-Brodsky, T. and Kaspi, Y.: Enhanced poleward propagation of storms under climate change, *Nat. Geosci.*, 10, 908–
556 913, <https://doi.org/10.1038/s41561-017-0001-8>, 2017.
- 557 Tang, Y., Han, Y., Ma, X., and Liu, Z.: Elevated heat pump effects of dust aerosol over Northwestern China during summer,
558 *Atmos. Res.*, 203, 95–104, <https://doi.org/10.1016/j.atmosres.2017.12.004>, 2018.
- 559 Tian, P., Zhang, L., Ma, J., Tang, K., Xu, L., Wang, Y., Cao, X., Liang, J., Ji, Y., Jiang, J. H., Yung, Y. L., and Zhang, R.:
560 Radiative absorption enhancement of dust mixed with anthropogenic pollution over East Asia, *Atmos. Chem. Phys.*, 18, 7815–
561 7825, <https://doi.org/10.5194/acp-18-7815-2018>, 2018.
- 562 Trenberth, K. E. and Stepaniak, D. P.: Covariability of Components of Poleward Atmospheric Energy Transports on Seasonal
563 and Interannual Timescales, *J. Climate*, 16, 3691–3705, [https://doi.org/10.1175/1520-0442\(2003\)016<3691:COCOPA>2.0.CO;2](https://doi.org/10.1175/1520-0442(2003)016<3691:COCOPA>2.0.CO;2), 2003.
- 565 University Corporation for Atmospheric Research (UCAR): WRF Source Codes and Graphics Software Downloads, UCAR
566 [code], https://www2.mmm.ucar.edu/wrf/users/download/get_source.html, last access: 1 May 2026.
- 567 Uno, I., Eguchi, K., Yumimoto, K., Takemura, T., Shimizu, A., Uematsu, M., Liu, Z., Wang, Z., Hara, Y., and Sugimoto, N.:
568 Asian dust transported one full circuit around the globe, *Nat. Geosci.*, 2, 557–560, <https://doi.org/10.1038/ngeo583>, 2009.
- 569 Voss, K. K. and Evan, A. T.: A New Satellite-Based Global Climatology of Dust Aerosol Optical Depth, *J. Appl. Meteorol.*
570 *Clim.*, 59, 83–102, <https://doi.org/10.1175/JAMC-D-19-0194.1>, 2020.
- 571 Wang, M., Lau, W. K. M., and Wang, J.: Impact of middle east dust on subseasonal-to-seasonal variability of the Asian summer
572 monsoon, *Clim. Dynam.*, 58, 2041–2057, <https://doi.org/10.1007/s00382-021-05694-z>, 2021.
- 573 Wang, Y., Jiang, J. H., and Su, H.: Atmospheric responses to the redistribution of anthropogenic aerosols, *J. Geophys. Res.-*
574 *Atmos.*, 120, 9625–9641, <https://doi.org/10.1002/2015JD023665>, 2015.
- 575 Wang, Y., Zhang, R., and Saravanan, R.: Asian pollution climatically modulates mid-latitude cyclones following hierarchical
576 modelling and observational analysis, *Nat. Commun.*, 5, 3098, <https://doi.org/10.1038/ncomms4098>, 2014a.
- 577 Wang, Y., Wang, M., Zhang, R., Ghan, S. J., Lin, Y., Hu, J., Pan, B., Levy, M., Jiang, J. H., and Molina, M. J.: Assessing the
578 effects of anthropogenic aerosols on Pacific storm track using a multiscale global climate model, *P. Natl. Acad. Sci. USA*, 111,
579 6894–6899, <https://doi.org/10.1073/pnas.1403364111>, 2014b.
- 580 Wang, Z., Huang, X., Wang, N., Xu, J., and Ding, A.: Aerosol-Radiation Interactions of Dust Storm Deteriorate Particle and
581 Ozone Pollution in East China, *J. Geophys. Res.-Atmos.*, 125, e2020JD033601, <https://doi.org/10.1029/2020JD033601>, 2020.
- 582 Xian, P., Klotzbach, P. J., Dunion, J. P., Janiga, M. A., Reid, J. S., Colarco, P. R., and Kipling, Z.: Revisiting the relationship
583 between Atlantic dust and tropical cyclone activity using aerosol optical depth reanalyses: 2003–2018, *Atmos. Chem. Phys.*,
584 20, 15357–15378, <https://doi.org/10.5194/acp-20-15357-2020>, 2020.
- 585 Xie, P. and Arkin, P. A.: Global Precipitation: A 17-Year Monthly Analysis Based on Gauge Observations, Satellite Estimates,
586 and Numerical Model Outputs, *B. Am. Meteorol. Soc.*, 78, 2539–2558, [https://doi.org/10.1175/1520-0477\(1997\)078<2539:GPAYMA>2.0.CO;2](https://doi.org/10.1175/1520-0477(1997)078<2539:GPAYMA>2.0.CO;2), 1997.



- 588 Xu, H., Guo, J., Wang, Y., Zhao, C., Zhang, Z., Min, M., Miao, Y., Liu, H., He, J., Zhou, S., and Zhai, P.: Warming effect of
589 dust aerosols modulated by overlapping clouds below, *Atmos. Environ.*, 166, 393–402,
590 <https://doi.org/10.1016/j.atmosenv.2017.07.036>, 2017.
- 591 Yin, Z., Wan, Y., Zhang, Y., and Wang, H.: Why super sandstorm 2021 in North China?, *Natl. Sci. Rev.*, 9, nwab165,
592 <https://doi.org/10.1093/nsr/nwab165>, 2022.
- 593 Yin, Z., Huo, Q., Hu, D., Huang, Y., and Wang, H.: Why record-breaking gale and nationwide dust in China in April 2025,
594 *Sci. Bull.*, 71, 463–465, <https://doi.org/10.1016/j.scib.2025.11.054>, 2026.
- 595 Yu, Y., Kalashnikova, O. V., Garay, M. J., and Notaro, M.: Climatology of Asian dust activation and transport potential based
596 on MISR satellite observations and trajectory analysis, *Atmos. Chem. Phys.*, 19, 363–378, [https://doi.org/10.5194/acp-19-363-](https://doi.org/10.5194/acp-19-363-2019)
597 2019, 2019.
- 598 Zeng, Y., Wang, M., Zhao, C., Zhu, Y., Rosenfeld, D., and Huang, K.-E.: Extremely High Concentrations of Ice Particles in
599 East Asian Dust-Infused Baroclinic Storm (DIBS) Cirrus Shield: Dominant Role of Dust Ice Nucleation Effect, *J. Geophys.*
600 *Res.-Atmos.*, 128, e2022JD038034, <https://doi.org/10.1029/2022JD038034>, 2023.
- 601 Zhang, R., Li, G., Fan, J., Wu, D. L., and Molina, M. J.: Intensification of Pacific storm track linked to Asian pollution, *P.*
602 *Natl. Acad. Sci. USA*, 104, 5295–5299, <https://doi.org/10.1073/pnas.0700618104>, 2007.
- 603 Zhang, X., Li, L., Che, H., Dubovik, O., Derimian, Y., Holben, B., Gupta, P., Eck, T. F., Lind, E. S., Toledano, C., Xia, X.,
604 Zheng, Y., Gui, K., and Zhang, X.: Aerosol Components Derived from Global AERONET Measurements by GRASP: A New
605 Value-Added Aerosol Component Global Dataset and Its Application, *B. Am. Meteorol. Soc.*, 105, E1822–E1848,
606 <https://doi.org/10.1175/BAMS-D-23-0260.1>, 2024.
- 607 Zhao, J., Ma, X., Wu, S., and Sha, T.: Dust emission and transport in Northwest China: WRF-Chem simulation and
608 comparisons with multi-sensor observations, *Atmos. Res.*, 241, 104978, <https://doi.org/10.1016/j.atmosres.2020.104978>, 2020.
- 609 Zhou, R. and Deng, Y.: A model analysis of the interactions between East Asian anthropogenic aerosols and North Pacific
610 atmospheric transients in boreal winter, *J. Geophys. Res.-Atmos.*, 118, 306–316, <https://doi.org/10.1029/2012JD018649>, 2013.
- 611 Zhou, T., Zhou, X., Yang, Z., Córdoba-Jabonero, C., Wang, Y., Huang, Z., Da, P., Luo, Q., Zhang, Z., Shi, J., Bi, J., and
612 Alikhodja, H.: Transboundary transport of non-east and East Asian dust observed at Dunhuang, northwest China, *Atmos.*
613 *Environ.*, 318, 120197, <https://doi.org/10.1016/j.atmosenv.2023.120197>, 2024.
- 614 Zhu, A., Ramanathan, V., Li, F., and Kim, D.: Dust plumes over the Pacific, Indian, and Atlantic oceans: Climatology and
615 radiative impact, *J. Geophys. Res.-Atmos.*, 112, D16208, <https://doi.org/10.1029/2007JD008427>, 2007.
- 616 Zhu, A., Xu, H., Deng, J., Ma, J., and Li, S.: El Niño–Southern Oscillation (ENSO) effect on interannual variability in spring
617 aerosols over East Asia, *Atmos. Chem. Phys.*, 21, 5919–5933, <https://doi.org/10.5194/acp-21-5919-2021>, 2021.
- 618